Seismic attenuation and mantle wedge temperatures in the Alaska subduction zone

Joshua C. Stachnik[1] and Geoffrey A. Abers
Department of Earth Sciences, Boston University, Boston, Massachusetts, USA

Douglas H. Christensen
Geophysical Institute, University of Alaska Fairbanks, Fairbanks, Alaska, USA

Received 12 February 2004; revised 22 June 2004; accepted 8 July 2004; published 8 October 2004.

[1] Anelastic loss of seismic wave energy, or seismic attenuation ($1/Q$), provides a proxy for temperature under certain conditions. The Q structure of the upper mantle beneath central Alaska is imaged here at high resolution, an active subduction zone where arc volcanism is absent, to investigate mantle thermal structure. The recent Broadband Experiment Across the Alaska Range (BEAAR) provides the first dense broadband seismic coverage of this region. The spectra of *P* and *SH* waves for regional earthquakes are inverted for path averaged attenuation operators between 0.5 and 20 Hz, along with earthquake source parameters. These measurements fit waveforms significantly better when the frequency dependence of Q is taken into account, and in the mantle, frequency dependence lies close to laboratory values. Inverting these measurements for spatial variations in Q reveals a highly attenuating wedge, with $Q < 150$ for *S* waves at 1 Hz, and a low-attenuation slab, with $Q > 500$, assuming frequency dependence. Comparison with *P* results shows that attenuation in bulk modulus is negligible within the low-Q wedge, as expected for thermally activated attenuation mechanisms. Bulk attenuation is significant in the overlying crust and subducting plate, indicating that Q must be controlled by other processes. The shallowest part of the wedge shows little attenuation, as expected for a cold viscous nose that is not involved in wedge corner flow. Overall, the spatial pattern of Q beneath Alaska is qualitatively similar to other subduction zones, although the highest wedge attenuation is about a factor of 2 lower. The Q values imply that temperatures exceed 1200°C in the wedge, on the basis of recent laboratory-based calibrations for dry peridotite. These temperatures are 100–150°C colder than we infer beneath Japan or the Andes, possibly explaining the absence of arc volcanism in central Alaska. *INDEX TERMS:* 7218 Seismology: Lithosphere and upper mantle; 3909 Mineral Physics: Elasticity and anelasticity; 5144 Physical Properties of Rocks: Wave attenuation; 8180 Tectonophysics: Tomography; 8124 Tectonophysics: Earth's interior—composition and state (1212); *KEYWORDS:* subduction zone, seismic attenuation, tomography

Citation: Stachnik, J. C., G. A. Abers, and D. H. Christensen (2004), Seismic attenuation and mantle wedge temperatures in the Alaska subduction zone, *J. Geophys. Res.*, *109*, B10304, doi:10.1029/2004JB003018.

1. Introduction

[2] In subduction zones, the presence of magmatism implies that temperatures must reach solidus conditions somewhere within the wedge. Some evidence suggests that melting conditions may prevail for much of the mantle wedge [*Kelemen et al.*, 2003], and melts of dry mantle may be common [*Elkins-Tanton et al.*, 2001], although the thermal structure of the wedge depends upon a number of dynamic and rheological factors [*Kincaid and Sacks*, 1997]. Seismic attenuation (described by a quality factor, Q) provides one tool for imaging temperature. At mantle conditions the attenuation of seismic waves occurs through a variety of temperature-dependent grain-scale processes [*Karato and Spetzler*, 1990], but Q is relatively insensitive to small degrees of partial melt or rock composition, unlike seismic velocities. Recently Q has shown promise as an imaging tool, and can vary spatially by a factor of 2–5, over tens of kilometers in subduction zones [e.g., *Eberhart-Phillips and Chadwick*, 2002; *Haberland and Rietbrock*, 2001; *Myers et al.*, 1998; *Roth et al.*, 1999; *Takanami et al.*, 2000; *Tsumura et al.*, 2000]. Such measurements of Q (or more commonly, $1/Q$) should provide insight into where temperatures may allow melting to take place.

[3] The Alaska segment of the Aleutian subduction system provides a useful test of melting theories. Although

[1]Now at Alaska Earthquake Information Center, Geophysical Institute, University of Alaska Fairbanks, Fairbanks, Alaska, USA.

0148-0227/04/2004JB003018$09.00

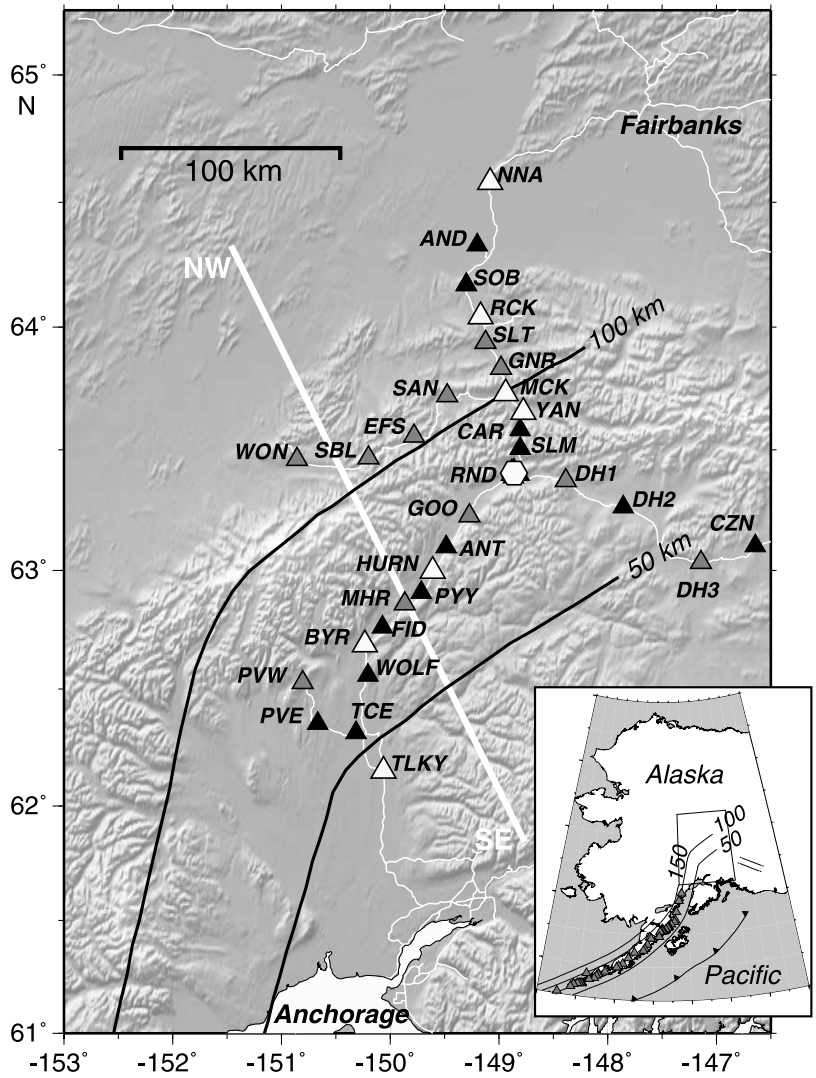

Figure 1. The BEAAR network and its setting. Triangles show seismic stations; open, operated June 1999 to September 2001; gray, operated June 2000 to September 2001; solid, operated June 2000 to September 2000. Hexagon shows site of six-element Reindeer array. Solid lines show isobaths to Wadati-Benioff zone [*Plafker et al.*, 1994]; white line shows cross section projection. Inset shows regional setting.

significant volcanism occurs in Alaska west of 152°W, and intermediate-depth seismicity continues as far east as 148°W (Figure 1), volcanoes are absent in central Alaska [*Plafker and Berg*, 1994]. The absence of arc volcanism in an otherwise normal subduction system provides a controlled experiment in understanding the causes of arc volcanism. Mantle melt is primarily governed by temperature and hydration; the lack of volcanism may be explained by anomalously low temperatures or by inadequate water flux. Alternatively, partial melt might exist at depth but remain unable to reach the surface for some reason related to crustal tectonics. These hypotheses predict different structures for the crust and mantle wedge, and hence different Q patterns.

[4] Because temperature varies in subduction zones over short distances, inferring temperature from Q requires a method that has high spatial resolution. Here, we measure Q from regional body waves and tomographically invert the resulting path-averaged Q measurements. We use P and S waves from intermediate depth earthquakes within the subducting Pacific plate to image the mantle wedge beneath central Alaska, supplemented by signals from upper plate earthquakes. The results show Q in the mantle wedge is similar to that of other subduction zones but higher, indicating somewhat colder temperatures than found beneath active volcanic arcs. These data also constrain the physical mechanism of attenuation, by confirming (or in some regions contradicting) laboratory derived properties of Q. Specifically, the Alaska measurements show good evidence for weak frequency dependence to Q in the 0.5–20 Hz range, a property required by laboratory measurements but rarely observed in a single data set. Also, they show that bulk attenuation in the mantle (but not the crust) is negligible compared with shear, consistent with high-temperature laboratory experiments. Thus these data confirm the

appropriateness of laboratory measurements of Q to predict temperature within the mantle wedge.

2. Attenuation Mechanisms

[5] Attenuation of seismic waves can be controlled by temperature, water content, and cracks or porosity of materials [*Karato and Spetzler*, 1990; *Mitchell*, 1995]. The attenuation of P and S waves, measured here as Q_P and Q_S, varies with attenuation of bulk and shear elastic moduli Q_κ and Q_μ, as

$$1/Q_P = (1 - R)/Q\kappa + R/Q\mu \quad (1a)$$

$$1/Q_S = 1/Q\mu \quad (1b)$$

where $R = 4V_S^2/3V_P^2$, and V_P, V_S are the P and S velocities, respectively [*Aki and Richards*, 1980]. At near-solidus conditions (temperatures above 900–1000°C), laboratory experiments show that seismic energy is dissipated through grain boundary interactions [*Sato et al.*, 1989] or intragranular relaxation [*Jackson et al.*, 2002, 1992; *Karato and Spetzler*, 1990], with $1/Q_\mu \gg 1/Q_\kappa$ for both mechanisms. Addition of small amounts of water, as hydrogen impurities in olivine crystals, may have the effect of lowering Q (increasing attenuation) in a manner indistinguishable from temperature changes [*Karato*, 2003], although direct measurements of this effect on Q have not yet been made. At temperatures substantially below solidus, it is likely that other processes attenuate seismic waves, including intergranular thermoelasticity and (at low pressures) deformation of cracks [e.g., *Budiansky et al.*, 1983; *Karato and Spetzler*, 1990; *Winkler and Nur*, 1979]. These latter processes can produce substantial $1/Q_\kappa$. Therefore the relationship of Q_P to Q_S should provide some insight into the attenuation mechanism, an approach which has indicated near-solidus conditions (i.e., $1/Q_\mu \gg 1/Q_\kappa$) beneath the Lau back arc [*Roth et al.*, 1999]. Some contribution from scattering to apparent attenuation may exist, particularly if $1/Q$ from these other processes is small.

[6] In laboratory studies, Q is found to be dependent on frequency [e.g., *Karato and Spetzler*, 1990], a property we confirm here with seismic data. Typically, the dependence is described as $Q \sim f^\alpha$ for frequency f. Experiments at high temperatures give $\alpha = 0.27$ for dunite at seismic frequencies [*Jackson et al.*, 2002], with older experiments generally showing $\alpha = 0.1–0.3$ [*Karato and Spetzler*, 1990]. This weak frequency dependence seems generally consistent with long-period variations in Q at mantle depths [e.g., *Warren and Shearer*, 2000]. By contrast, crustal studies show strong frequency dependence ($\alpha > 0.5$), using *Lg* and coda waves (1–20 Hz) [e.g., *Benz et al.*, 1997; *McNamara*, 2000] or body waves in continental crust (1–25 Hz) [e.g., *Sarker and Abers*, 1998a]. The physical mechanism of such strong frequency dependence is unclear, but probably depends upon the presence and deformation of cracks or pores [*O'Connell and Budiansky*, 1977; *Winkler and Nur*, 1979]. Although most attenuation mechanisms indicate some frequency dependence, most measurements of Q with body waves typically fix $\alpha = 0$, usually because frequency dependence often cannot be resolved over limited frequency ranges [e.g., *Flanagan and Wiens*, 1994; *Schlotterbeck and Abers*, 2001; *Takanami et al.*, 2000]. In two exceptions, *Flanagan and Wiens* [1998] showed that $\alpha = 0.1–0.3$ in the upper mantle beneath the Fiji Plateau, would reconcile several studies over 0.1–8 Hz, and *Shito et al.* [2004] found $\alpha = 0.2–0.4$ in the Izu back arc from regional P wave spectra.

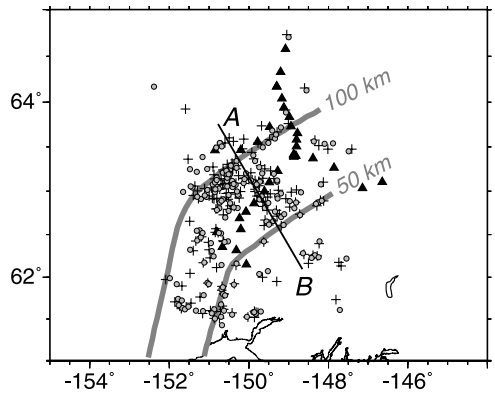

Figure 2. Events used. Crosses show original catalog locations; solid circles show relocated epicenters; triangles show BEAAR stations; thick gray lines show 50 and 100 km slab isobaths; thin line shows location of cross section in Figure 3.

3. Data and Methods

3.1. Experiment

[7] From June 1999 through August 2001 we deployed the Broadband Experiment Across the Alaska Range (BEAAR), an array of 36 IRIS/PASSCAL broadband instruments across central Alaska (Figure 1). During the deployment, seven instruments at 50 km spacing operated for the full 28 months, an additional 10 stations operated for 15 months, and all 36 stations operated for 4 summer months. For this study we analyze data only from the 4 summer months in 2000 during which the entire network operated. Data derive from RefTek 72A-08 24-bit digitizers, operating at 50 samples/s, recording signals from three-component broadband instruments (Guralp CMG-3T and CMG-3ESP sensors). This configuration yields a flat velocity response between frequencies of 0.0083 and 20 Hz, here corrected for instrument gain and integrated to displacement. All stations had clock times and station locations determined by GPS.

3.2. Hypocenters and Velocities

[8] We analyze here regional earthquakes >50 km deep that sample the slab and wedge beneath BEAAR, supplemented with 24 events in the upper plate crust. Preliminary earthquake locations are derived from monthly catalogs produced by the Alaska Earthquake Information Center (AEIC) from June to September 2000 using their automatic detection and location system [*Lindquist*, 1998]. These arrival times are supplemented with P and S times picked from BEAAR records, then jointly inverted for relocated hypocenter and one-dimensional velocity structure following *Roecker* [1993]. The resulting data set includes 178 hypocenters up to 140 km deep (Figures 2

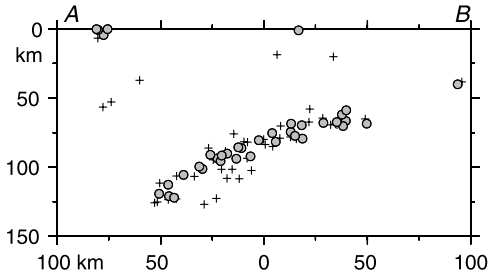

Figure 3. Cross section of hypocenters relocated using BEAAR arrival times. Crosses show original catalog locations; solid circles show relocated epicenters. Cross section is located on Figure 2.

and 3), and eight-layer P and S velocity model. Mantle P velocities lie in the range 7.80–8.05 km/s. The relocations reduce the scatter of the Benioff zone seismicity so that events depart by only a few km from a single surface, with no events elsewhere at mantle depths. Receiver functions show that these events all lie immediately beneath the slab surface, probably within subducted crust [*Ferris et al.*, 2003].

3.3. Waveforms and Spectra

[9] We analyze body wave spectra of regional events from the vertical component for P waves and the transverse component for S waves (to minimize P-to-S mode conversions off horizontal discontinuities). Multitaper spectra [*Park et al.*, 1987] are calculated from these signals in windows 3 s in duration, beginning 0.5 s before the arrival pick, then corrected for instrument gain and converted to displacement. Body waves from slab events typically show short duration, so these windows include all of the main pulse of the waveform; signals were excluded where significant P or S energy extended past the windows. Tests showed that increasing the window length to 4–6 s produced insignificantly different spectra or attenuation measurements; the latter agreed with those derived for a 3 s window with correlation coefficient of 0.93 and no significant bias. The longer windows occasionally included secondary phases, so the 3 s windows are favored.

[10] We calculate noise spectra from a 3 s long window immediately preceding each signal window (Figure 4). For S, the noise window consists of late P coda. The frequency band fit varies according to signal-to-noise levels (Figure 4 and Table 1), typically between 0.25 and 20 Hz, in order to maximize information content. Low-Q paths give S waves above noise only at frequencies below 5–10 Hz, while spectra from high-Q paths show little effect on amplitudes except at frequencies above 5–10 Hz. While a narrower

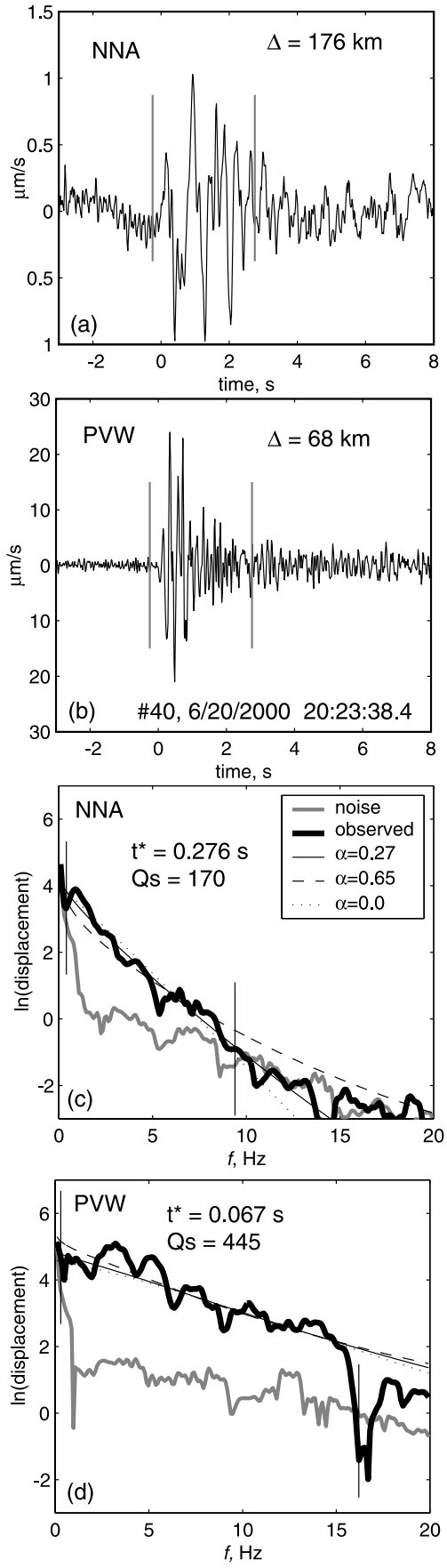

Figure 4. Spectral fitting example with S waveforms. (a) S waves at a northern station (NNA) and (b) at a southern station (PVW) from an event 110 km deep. Δ shows distance to stations. (c) and (d) Multitaper amplitude spectra of same signals corrected to displacement (black line) or of noise in 3 s window immediately preceding (gray line). Thin lines show best fit model following equation (2) for α as labeled. Vertical lines show window being fit on all panels. Note lack of high-frequency energy at NNA, typical of wedge paths.

Table 1. Path-Averaged Q Estimates

Path	Phase	Q_o	Error[a], %	Q_{av}	Error,[a] %	Number of Data	nVar[b]	$Q_{av\text{-}cor}$[c]	Error,[a] %	f_{min},[d] Hz	f_{max},[d] Hz
						$\alpha = 0.27$					
Crust	P	291	10	242	5.0	446	0.33			0.4	19.2
Wedge	P	764	66	257	4.5	340	0.41	266	19	0.8	19.1
Slab	P	∞[e]	-	793	10.3	515	0.87	∞[e]	-	1.0	19.2
Crust	S	3445	82	317	5.7	398	0.28			0.3	13.9
Wedge	S	174	12	173	2.4	286	0.13	138	7.7	0.3	9.4
Slab	S	4308	136	497	4.1	503	0.47	724	53	0.4	16.9
						$\alpha = 0.0$					
Wedge	P	1696	63	528	4.0	340	0.37	537	36	0.8	19.1
Wedge	S	252	11	348	3.0	286	0.17	283	20	0.4	9.4
						$\alpha = 0.65$					
Wedge	P	1213	328	93	5.0	340	0.45	104	6.6	0.9	19.1
Wedge	S	94	15	73	2.5	286	0.13	62	2.6	0.4	9.4

[a]Formal uncertainty (1σ) in $1/Q$ is from regression for $1/Q_o$ or $1/Q_{av}$, expressed as percent.
[b]Variance of misfit to t^* data is for the Q_o regression, normalized to variance in t^* measurements.
[c]Q_{av} is corrected for attenuation in the crust.
[d]The f_{min} and f_{max} are mean minimum and maximum frequency bounds in t^* measurements.
[e]The $1/Q$ estimate is negative, but uncertainties include zero.

band has an advantage of consistency, a wide frequency band is necessary to analyze wide ranges in Q. In one test, in which all spectra were limited to $f < 8$ Hz, Q_P and crustal Q increased in variance by several times relative to the results from all frequencies, and were essentially unusable. The mantle Q_S remained well constrained. For the upper plate events, only path lengths less than 150 km long are used in location, to avoid *Pn* contamination. For all events, paths are short and generally upgoing; 50% of source-receiver ranges are <100 km and 90% of paths are <190 km long. Slab events range from 40 to 135 km depth. Because these ray paths are upgoing and exit the slab rapidly, three-dimensional ray bending effects should be minor throughout the wedge.

[11] Of the 178 earthquakes relocated, 102 have good signals on 6 or more stations and form the basic attenuation data set. These earthquakes range in moment-magnitude (M_w) 2.1 to 4.7, corresponding to corner frequencies ranging from 2 to >20 Hz. Earthquakes are small and show a wide variation in focal mechanism, so directivity effects are likely to be minor and unsystematic.

4. Attenuation Measurements

4.1. The Parameter t^* From Parametric Inversions

[12] Following common practice [e.g., *Schlotterbeck and Abers*, 2001], we measure path-averaged attenuation as $t^* = \tau/Q$, for travel time τ. A displacement spectrum recorded at station j from earthquake k, $A_{jk}(f_i)$, can be approximated as [e.g., *Anderson and Hough*, 1984]

$$A_{jk}(f_i) = \frac{C_{jk} M_{0k} \exp\left(-\pi f_i t^*_{jk}\right)}{1 + (f_i/f_{ck})^2} \quad (2)$$

where f_i is the ith frequency sampled, M_{0k} and f_{ck} are the seismic moment and corner frequency, respectively, for the kth event, C_{jk} accounts for frequency-independent effects such as geometrical spreading, radiation pattern and elasticity, and t^*_{jk} is the attenuation operator. This model does not include frequency-dependent site amplification and assumes a simple f^2 source spectrum, consistent with most previous studies. We calculate C_{jk} from geometrical spreading, free surface and source excitation effects consistent with the one-dimensional velocity model, and approximate the P and S radiation patterns by their spherical average [*Aki and Richards*, 1980].

[13] To determine the parameters, all spectra for event k are jointly inverted for a single M_{0k} and f_{ck}, and for separate t^*_{jk} along each path. The source parameters are determined separately for P and S, because the f_{ck} may differ with phase [e.g., *Madariaga*, 1976]. To show the form of this inversion, equation (2) can be rewritten as a set of equations for several i, j:

$$\ln\{A_{jk}(f_i)\} + \ln\left\{1 + (f_i/f_{ck})^2\right\} - \ln\{C_{jk}\} = \ln\{M_{0k}\} - \pi f_i t^*_{jk}. \quad (3)$$

The left-hand side of these equations contain the observed displacement spectra $A_{jk}(f_i)$ for the M stations ($j = 1, \ldots, M$) which record event k, corrected for source (f_{ck}) and frequency-independent propagation effects (C_{jk}). Each spectrum is sampled continuously (at 50/512 Hz interval) at the N frequencies ($i = 1, \ldots, N$) for which signal-to-noise levels are high, so N varies from record to record. For event k, this forms a system of NM equations for $M + 2$ parameters $\ln\{M_{0k}\}$, f_{ck}, and M values t^*_{jk}. To solve the nonlinear part of this problem, a sequence of values for f_{ck} is tested from 0.25 to 50 Hz at 0.25 Hz intervals. At each f_{ck} the remaining linear system of equation (3) is solved for $\ln\{M_{0k}\}$ and t^*_{jk}. The f_{ck} producing the lowest misfit between left- and right-hand sides of equation (3) in the least squares sense is chosen. These measurements of t^*_{jk} are termed parametric because the results depend upon a parameterized description of source effects.

[14] The standard errors calculated from the linear part of the problem become the formal uncertainties in the resulting t^*_{jk} used for subsequent tomographic inversions. Such uncertainties account for noise in observations but neglect trade-off with uncertainty in f_{ck}, which is fixed in the linear inversion. They also implicitly assume that each $A(f_i)$ are independent, which is unlikely for windowed multitaper

spectra, so underestimate actual errors. An approximation, discussed below, accounts for these additional sources of error in the tomographic inversion by treating them as errors in theory [*Tarantola and Valette*, 1982].

[15] A correction is made to account for frequency-dependent site effects. The residual spectra (difference between left- and right-hand sides of equation (3)) for each station are averaged over all events, smoothed, and subtracted from the observed spectra. Then, the entire inversion procedure is repeated, to derive final t^*_{jk} estimates. Also, three stations showing large site effects (DH1, MHR, TCE) were not used to determine f_c. Results for S show little sensitivity to site corrections, although the P results in the upper plate crust show some differences. Finally, only those signals showing signal-to-noise ratios above 2.5 for both S and P were kept, so that the data set has matching S and P observations.

[16] These procedures and subsequent outlier removal produce a total of 2318 t^*_S measurements and 2066 t^*_P measurements, used for path-averaged estimates. Of these, 2004 had common station-event pairs for P and S, and were used in tomographic inversion. For $\alpha = 0$ (see below), median t^* is 0.0247 s for P and 0.0474 s for S, but both vary by an order of magnitude with median formal errors of 0.0016 s and 0.0024 s, respectively. The f_c for P systematically exceeds those for S by a factor of 1.5, consistent with a variety of source models [*Madariaga*, 1976]. Seismic moments for S and P correlate well (correlation coefficient = 0.93 with no significant bias), and correlate well with catalog magnitudes [*Stachnik*, 2002]. Thus the inversions recover reasonable source parameters.

4.2. Potential Distortion of Spectra

[17] The presence of a low-velocity layer atop the subducting slab, possibly representing subducted oceanic crust, has been shown to exist under central Alaska [*Abers and Sarker*, 1996; *Ferris et al.*, 2003]. Because such a layer acts as a frequency-dependent waveguide, the observed spectrum for certain paths could be modeled incorrectly. A waveguide enhances high frequencies, so should decrease the apparent attenuation. We exclude signals that exhibit obvious dispersion by visual inspection, and exclude ray paths with long segments along the top of the slab. Still, some measurements of small (or negative) t^* may be influenced by focusing, particularly along the slab. The unusual parts of the slab we observe have high not low attenuation, so cannot be explained by this mechanism.

[18] Errors in f_c may trade off with t^*, as both parameters affect spectral falloff [*Anderson*, 1986]. Several results suggest that this trade-off does not produce significant biases here in source parameters, and by inference in t^*. First, our f_c estimates appear reasonable; they give stress drops comparable with those elsewhere (e.g., 1–10 MPa) and are similar for P and S [*Stachnik*, 2002]. Second, the seismic moments estimated here are consistent with those derived from M_L magnitudes for Alaska earthquakes after correcting for known path biases [*Lindquist*, 1998; *Stachnik*, 2002]. Third, in several tests we reinverted all spectra with different assumptions about the source, and the resulting attenuation estimates show no systematic changes. These tests include (1) f_c fixed a priori from the earthquake magnitude and assumed stress drop (10 MPa); (2) f_c arbitrarily set to 40 Hz, well outside the range of fits; (3) earthquakes restricted to those with $M < 2.2$, a size for which corner frequencies should significantly exceed the range of frequencies sampled (see section 4.4); and (4) a source model with sharper corner, in which the denominator in equation (2) is changed to $[1 + (f/f_c)^4]^{1/2}$ [*Abercrombie*, 1995]. In all of these tests, the resulting changes to attenuation lie inside the calculated uncertainties. Overall, while errors in source parameterization may contribute to uncertainties, they do not seem to significantly bias the estimated attenuation.

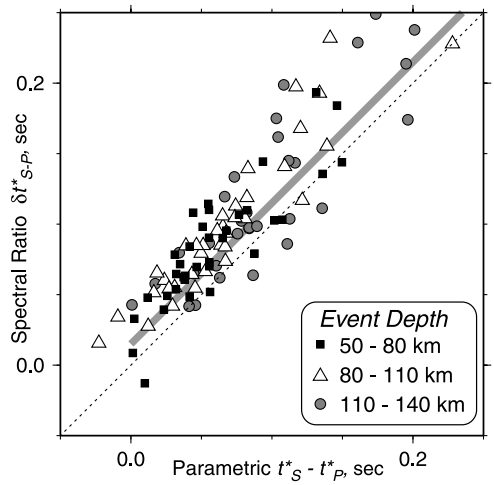

Figure 5. Comparison of δt^* to parametric estimates of $t^*_S - t^*_P$. Each symbol represents average measurement for one station over events in one depth range (symbol). Dashed line shows 1:1 relationship, gray line shows estimated bias in δt^* if P and S corner frequencies differ by a factor of 1.5, as expected [*Madariaga*, 1976]. Similarity of two axes indicates that the parametric method accounts for source effects adequately.

4.3. Q From S-to-P Spectral Ratio

[19] As a check on the parametric measurement of t^* (equation (3)), we also estimate Q from the spectral ratio of S to P waves, an approach which should approximately remove source, site and instrument effects [e.g., *Roth et al.*, 1999]. The method gives estimates of $\delta t^* = t^*_S - t^*_P$, which require assumptions about Q_P/Q_S to interpret, a quantity which we find varies greatly. The overall pattern of attenuation inferred from δt^* resembles that from t^*_S, and gives similar estimates of Q_S for highly attenuating wedge paths; the similarity can be seen by comparing δt^* to parametric estimates of $t^*_S - t^*_P$ (Figure 5). Uncertainties are similar for the two techniques; suites of δt^* measurements from event clusters to individual stations show statistical variance that is comparable to that of parametric t^*_S or t^*_P. This similarity in variance may indicate that trade-offs between t^*_S and f_c, presumably eliminated in δt^*, are not a major source of error. A small bias between δt^* and $t^*_S - t^*_P$ may result from the assumption that f_c is the same in P and S in the ratio technique. Also, at high t^*, the t^*_P appears slightly underestimated. A positivity constraint applied to tomography (see below) removes this slight shift. Because no major biases could be found between the two sets of results, and

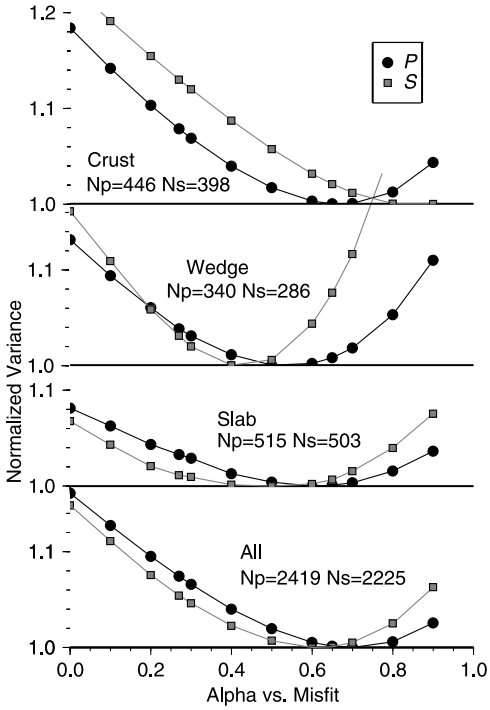

Figure 6. Variance of misfit to spectra summed over data set, as a function of frequency dependence parameter α, normalized to minimum variance value for phases shown. *Np* and *Ns* give number of records used for *P* and *S*, respectively.

interpretation of δt^* requires assumptions about Q_P/Q_S, we do not discuss these results further.

4.4. Frequency Dependence

4.4.1. Estimation of α

[20] Physical mechanisms of attenuation can be potentially discriminated by their frequency dependence, described by

$$t^* = t_o^* f^{-\alpha} \tag{4}$$

where t_o^* represents attenuation at 1 Hz. We constrain this frequency dependence substituting equation (4) into equations (2) and (3), then invert each spectra for t_o^* in the manner described above, but with α fixed at values from 0.0 to 1.0 at 0.1 increments. The α is estimated by minimizing the global variance of the misfit for large data subsets (Figure 6). For simplicity, t_o^* is referred to as t^* in subsequent discussions.

[21] We estimate α for the entire data set and for three subsets: (1) paths that sample upper plate crust (paths from sources <40 km deep); (2) mantle wedge paths (sources >85 km deep, north of 63°N, west of 149°W, to stations north or west of MCK), and (3) slab paths (same events as wedge, but to stations south or east of RND). For the entire data set, α = 0.7 or 0.6 fit *P* or *S* best, respectively, and similar values are found for crustal paths (Figure 6). The independent estimate of α = 0.66 at 1–20 Hz from crustal *Lg* phases in central Alaska [*McNamara*, 2000] agrees closely, indicating that the frequency dependence is robust and well constrained, and that similar processes likely attenuate both body waves and *Lg*. Values of α near 0.65 typify many tectonically active areas [*Mitchell*, 1995].

[22] By comparison, both wedge and mantle paths show significantly lower values of α, near 0.4–0.5 in the wedge and slightly higher for slab paths (Figure 6). These mantle paths sample the crust for roughly one third of their length, for which α = 0.6–0.7. Hence attenuation in the mantle must then exhibit somewhat less frequency dependence than α = 0.4–0.5, likely close to the α = 0.27 indicated by high-temperature laboratory experiments [*Jackson et al.*, 2002; *Karato*, 2003]. In the wedge these experiments should have most relevance, so it is reassuring that the observed frequency dependence agrees with that predicted for high-temperature mantle rock. *Flanagan and Wiens* [1998] and *Shito et al.* [2004] observe similar α for back arc paths.

[23] It is possible that the inferred frequency dependence represents some bias in the fitting procedure, rather than real frequency dependence, but several tests suggest otherwise. Increasing α decreases the rate at which amplitudes decay with increasing frequency, an effect which may be mimicked by errors in the description of the source spectra. To test this effect, we recalculated α using only the 33% of the data set corresponding to small events (M_L < 2.2), which should have corner frequencies above the frequency band being studied. The results show nearly identical minima in variance of misfit with α, indicating that a source parameterization error is not producing apparent frequency dependence. In two related tests, we fixed f_c to an arbitrary high value, and to a value predicted from the local magnitude assuming constant stress drop. The results show greater scatter, but no systematic change in α.

4.4.2. Implications for Comparing Q From Different Studies

[24] Attenuation estimates at 1 Hz (from t_o^*) vary systematically with α, such that larger α gives lower Q at 1 Hz (Figure 7 and Table 1). Estimates of Q at different α

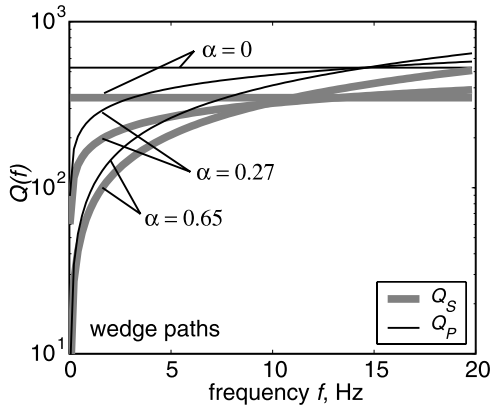

Figure 7. Variations in path-averaged Q with frequency for the mantle wedge (Q_{av}, Table 1) for varying α. *S* waves (thick lines) all give similar Q near f_R = 10 Hz for any α, while *P* waves (thin lines) give same values near f_R = 15 Hz. The maximum frequencies sampled (f_{max}, Table 1) lie near f_R, indicating that the greatest sensitivity to Q lies at the highest frequencies used.

converge above 1 Hz, such that the estimates for all α converge at a common frequency, f_R, for any given data subset. The common frequency f_R lies at the high end of the frequency band sampled, near 10–20 Hz depending upon path (f_{max} in Table 1), a pattern which indicates that these measurements are most sensitive to attenuation near f_{max}. This seems reasonable, as the amplitude reduction of spectra relative to a nonattenuating signal should be greatest at highest frequencies. In other words, any similar measurements of Q, particularly those assuming no frequency dependence, mostly reflect Q at the upper end of the frequency band sampled. We suspect this is true of any measurement of attenuation based upon spectral falloff [e.g., *Haberland and Rietbrock*, 2001; *Roth et al.*, 1999; *Tsumura et al.*, 2000]. Some of the variation between studies may just reflect this difference in sample frequencies, and the frequency dependence of Q. Thus spectra-based measurements of Q cannot be compared without knowing something about the frequency band of measurement.

[25] One consequence of this phenomenon is that frequency-independent estimates will tend to systematically overestimate Q (underestimate attenuation) at frequencies below f_R. Applications of such Q estimates, for example in predicting seismic hazards, should take this effect into account.

4.4.3. Comparing Results for Different α

[26] Both path-averaged Q measurements and tomographic estimates show similar patterns for all assumed α, so results for one value of α should be predictable from another. Rather than present results for all α in detail, we present results for $\alpha = 0.27$ only, a value most appropriate for the mantle wedge. Results for other α can be derived as follows. Figure 7 shows that at some frequency, f_R, the t^* estimates for all α will agree. Then

$$Q_1(\alpha) = Q_1(0)(f_R/1\ \text{Hz})^{-\alpha} \quad (5)$$

where $Q_1(\alpha)$ represents a path-averaged Q estimate at 1 Hz for a given α, and $Q_1(0)$ is the frequency-independent estimate. This relationship best fits the entire data set for $f_R = 13$ Hz; however, f_R varies with Q. The signal-to-noise ratio at high frequencies decreases with decreasing Q (greater spectral falloff), so f_R decreases with decreasing Q, approximately as

$$f_R = aQ_1(0)^k \quad (6)$$

for constants a and k. Regression of S wave t^* measurements gives $k = 0.505 \pm 0.012$ and $\ln(a) = -0.64 \pm .08$, for f_R in Hz (1σ uncertainties). This relationship can explain 90.5% of the variance in $Q_1(\alpha > 0)$ relative to $Q_1(0)$.

4.5. Path-Averaged Q

[27] We estimate path-averaged attenuation for several sets of station-event combinations from parametric t_S^* and t_P^* measurements (Table 1). These estimates provide robust measurements averaged over large regions, and serve as a check on tomographic results. The simplest such average is $1/Q_{av} = t^*/\tau$, where τ is travel time, a measure which shows strong spatial variations for mantle paths (Figure 8). In some situations near-surface attenuation might be significant [e.g., *Hough et al.*, 1988], which we approximate as $t^* = t_R^* + \tau/Q_o$. The $1/Q_o$ estimates then describe attenuation along the path, while t_R^* describes attenuation contributions common to all paths, such as near-surface effects.

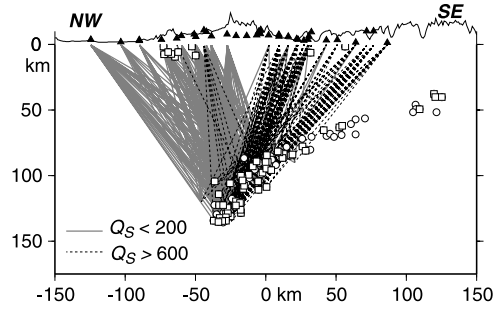

Figure 8. Path-averaged Q_{av} for S, from events greater than 85 km deep north of 63°N. Rays are projected onto cross section illustrated on Figure 1 and shaded according to Q ($\alpha = 0.27$). Topography, top, is exaggerated 10 times. Solid triangles show stations; open symbols show relocated events, squares if used in inversions.

[28] We calculate attenuation for three subsets of data, crust, mantle wedge, and slab (Table 1), as defined in section 4.4.1. For each subset and phase, $1/Q_{av}$ and $1/Q_o$ are calculated by regression. The $1/Q_{av}$ estimates appear robust for all paths. For $1/Q_o$, stable results are only obtained for crustal P paths and wedge S paths, where formal errors are 10–12%; elsewhere, formal errors are 28–200%, in part because these averages neglect lateral variations in parameters. Both methods give similar Q_S for the wedge, 170–180 at $\alpha = 0.27$. Attenuation in the wedge is much greater than in the slab, by a factor of 3–20 for S and, for the Q_{av} method, nearly a factor of 3 for P. This observation is consistent with the overall low frequency content seen in mantle-wedge signals (Figure 4). The boundary between high- and low-Q_S regions is sharp and lies near the south flanks of the main Alaska Range (Figure 8).

[29] To remove the effect of the crust on Q_{av} within the mantle, we approximate the crust and mantle contributions as

$$Z/Q_{av} = Z_c/Q_c + (Z - Z_c)/Q_{av-cor} \quad (7)$$

where Z is the median earthquake depth for a group of events, Z_c is the crustal thickness, and Q_c is the crustal attenuation, and $Q_{av\text{-}cor}$ is the corrected wedge attenuation. For the "slab" and "wedge" paths in Table 1, $Z = 112$ km, $Z_c = 40$ km [*Meyers-Smith et al.*, 2002], and Q_c can be taken from Q_{av} for crustal paths. The correction gives $Q_{av\text{-}cor}$ of 138 (±7.7%) for S ($\alpha = 0.27$), and using equation (1) gives bulk attenuation of $Q_\kappa = 757$ for $V_P/V_S = 1.80$. Hence shear attenuation dominates bulk attenuation in the wedge, as expected.

5. Tomographic Inversion

5.1. Method

[30] We invert the t^* measurements for three-dimensional variations in $1/Q$. The method, described in detail previously [*Sarker and Abers*, 1998b; *Schlotterbeck and Abers*, 2001], is summarized here emphasizing improvements. We

approximate heterogeneity by blocks of constant velocity V and $1/Q$. Then t^* for the ith ray path is

$$t_i^* = \sum_j l_{ij}/V_j Q_j \quad (8)$$

where l_{ij} is the path length of the ith ray in the jth block and V_j and $1/Q_j$ are the velocity and attenuation parameter, respectively, of block j. To the extent that V can be constrained independently of $1/Q$, a linear relationship then exists between $1/Q_j$ and t_i^*, that can be inverted. (Physical dispersion introduces some coupling [*Karato*, 1993], but the effects of these velocity variations on t^* are negligible.) For simplicity, rays are traced in a one-dimensional velocity model.

[31] The inversion of the t_i^* for $1/Q_j$ follows the maximum-likelihood linear inverse theory of *Tarantola and Valette* [1982]. In the absence of observations, results are constrained to an a priori model PREM [*Dziewonski and Anderson*, 1981], modified to include a lossy near-surface layer (Q_S = 50 in the upper 500 m). The a priori model uncertainties are set to 100% in $1/Q$, and we do not include any smoothness constraints other than finite block size, as the data are well behaved. Uncertainties in observations are assumed to be those determined from the t^* measurements, treated as Gaussian. To account for unmodeled errors in the t^* measurements (see section 4.1), the inversion includes an a priori uncertainty in theory σ_T, which quantifies errors in the theoretical relationships used to predict observations [*Tarantola*, 1987]. The σ_T incorporates errors due to finite block size, to errors in f_c and the source model generally, and to other approximations in the theory used to predict $1/Q$. We set σ_T = 0.03 s for all observations being fit, derived from the measured variation in t^* over collocated clusters of events (for details, see *Stachnik* [2002]).

[32] Initial inversions showed that, for a few poorly resolved blocks, $1/Q_P < 0.41/Q_S$, giving the nonphysical result that $1/Q_\kappa < 0$ (equation (1), for V_P/V_S = 1.80 as in PREM). However, larger $1/Q_P$ could fit the data nearly equally well. To enforce the physical constraint that $1/Q_\kappa \geq 0$, the final inversions for $1/Q_P$ include an iterative step which adjusts those nodes which $1/Q_P < 0.41/Q_S$, by simultaneously increasing their damping and reducing their a priori $1/Q_P$ toward $0.41/Q_S$. No more than three iterations are necessary in most cases to enforce the $1/Q_\kappa \geq 0$ constraint for all but one or two nodes. The resulting models have the benefit that $1/Q_\kappa$ everywhere is nonnegative, and that trade-offs between damped and undamped blocks are handled correctly. This procedure increases global variance of misfit in P by only 4.8% relative to inversions with no positivity constraints, less than the variance change associated with minor changes to grid geometry. We use $1/Q_{Pu}$ to denote P results from the unconstrained inversion, and $1/Q_{Pc}$ to denote inversions for which $1/Q_\kappa$ is constrained to be positive. A similar process enforces $1/Q_S > 0$ for all blocks, although almost no well-resolved nodes are affected.

5.2. Inversion Parameterization

[33] We take two approaches to parameterization, one emphasizing resolution of small features, and another "minimum parameterization" method designed to recover $1/Q$ averages with high accuracy. The first follows the standard approach of dividing the earth into small cells of constant $1/Q$, and inverting for them. A top layer accounts for near-surface effects, extending beneath each station to 500 m below sea level, with 10 km horizontal grid spacing so that each station lies on a separate block. Such a layer allows expected high near-surface attenuation [e.g., *Hough et al.*, 1988]. Below this layer, the inversion grid is broken into regular cells in both crust and mantle, 20 km wide across strike but much longer along strike (Figure 9). Horizontal boundaries include a Moho at 40 km depth, as indicated by receiver functions [*Ferris et al.*, 2003; *Meyers-Smith et al.*, 2002], and others at 20 km intervals. A sequence of across-strike block widths was tested, for spacings of 10–50 km, and 20 km was the smallest size to significantly reduce variance over larger blocks. We express results as $1000/Q$, for convenience.

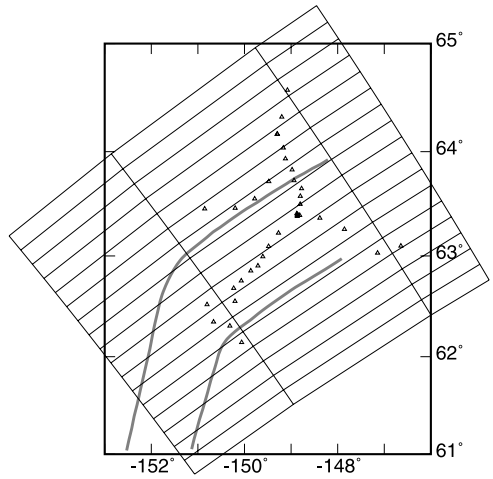

Figure 9. Grid used for $1/Q$ inversions, showing constant Q blocks, for all depths except the near-surface. Triangles show stations; thick gray lines show 50 and 100 km slab isobaths.

5.3. Inversion Results

5.3.1. Overview

[34] Inversions show high $1000/Q_S$ (high attenuation) in the mantle wedge and generally low $1000/Q_S$ in both upper plate crust and downgoing slab (Figure 10). The high $1000/Q_S$ wedge exists only where the slab is deeper than 80 km, and shows an abrupt termination to the SE where the slab shallows. The highest attenuation in the wedge has $1000/Q_S$ = 7–10 (Q_S = 100–140) for α = 0.27, with standard errors near 1.0, in accord with path-averaged estimates (Table 1). This high attenuation dominates the signals (e.g., Figures 4a and 4c). The upper plate crust shows $1000/Q_S < 2.5$, and the slab below 75 km depth shows even less attenuation ($1000/Q_S < 1.0$). Unexpectedly, the slab shows relatively high attenuation at depths less than 80 km, $1000/Q_S$ = 2.5–5.5. This region appears to be well resolved and can be recovered from inversions of small subsets of the data with limited ranges of path length.

[35] The P results differ substantially from S. Crust shows high attenuation, while the mantle wedge shows little. The Q_{Pu} image has a region of almost no attenuation immediately above the slab at 50–100 km depth, a

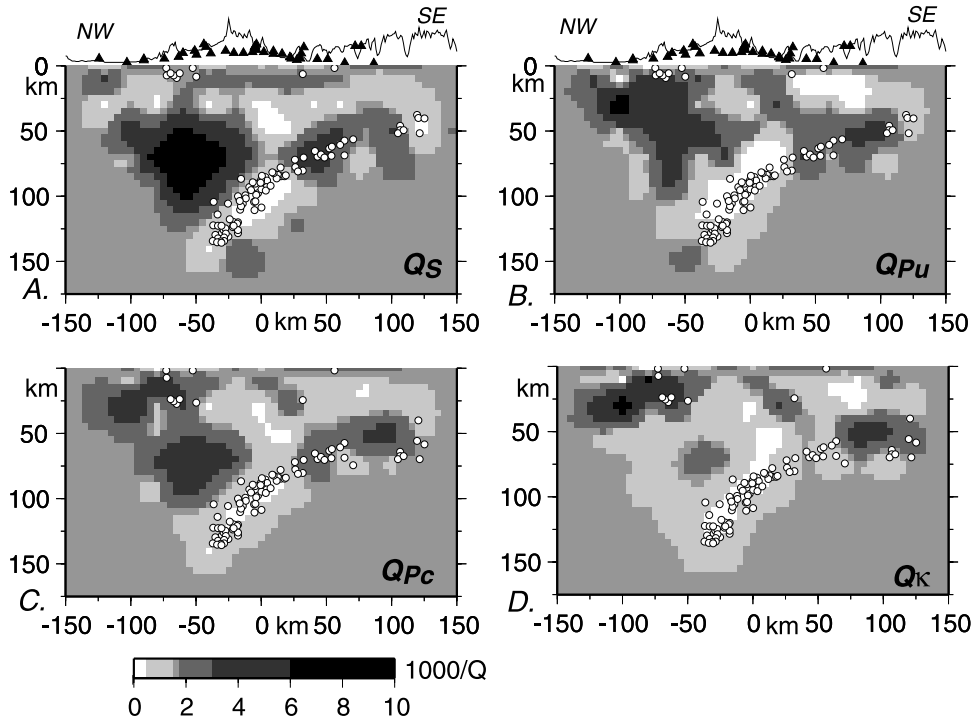

Figure 10. Results of tomographic inversion in cross section (Figure 1): (a) $1000/Q_S$, (b) $1000/Q_P$ with no constraints, (c) $1000/Q_P$ constrained so that $1000/Q_\kappa$ is nonnegative, and (d) resulting bulk modulus attenuation $1000/Q_\kappa$, from equation (1). Circles show events; triangles show stations projected onto cross section. Elevations and topography are exaggerated 10 times. White corresponds to a priori model, $1000/Q = 1.67$ ($Q = 600$). See color version of this figure at back of this issue.

feature which becomes less pronounced in Q_{Pc}. Still, $1000/Q_\kappa$ is generally low in the mantle (<1.0) and 2–5 times higher in the crust. Both $1000/Q_S$ and $1000/Q_\kappa$ show the high-attenuation region within the slab at <80 km depth, discussed below.

[36] Crustal attenuation lies in the range $1000/Q_S = 1–3$, averaging 1.3. *McNamara* [2000] found $Q_S = 220$ from *Lg* coda at 1 Hz, and $\alpha = 0.66$, equivalent to $1000/Q_S = 1.4$ at $\alpha = 0.27$ following equations (5) and (6), consistent with the measurements here. Our $1000/Q_P$ is somewhat higher, giving $1000/Q_\kappa \sim 5–7$ directly beneath the northernmost stations. The high $1000/Q_\kappa$ may reflect unusual basin effects, as these stations lie on the Central Tenana Basin sediments, 2 km thick including up to 1 km of Pliocene gravels [*Kirschner*, 1994]. High P wave attenuation typifies many crustal studies in tectonically active areas [e.g., *Mitchell*, 1995; *Rautian et al.*, 1978; *Schlotterbeck and Abers*, 2001], probably a combination of poroelastic and scattering effects.

[37] Attenuation for the near-surface layer, representing site effects, ranges from $1000/Q = 10–120$, with medians of 28 and 35 for P and S, respectively. These values are an order of magnitude greater than $1000/Q$ for the blocks immediately below, consistent with the a priori assumptions and with estimates for weathered layers elsewhere [*Abercrombie*, 1997; *Aster and Shearer*, 1991].

5.3.2. Formal Resolution and Uncertainty

[38] For both $1000/Q_{Pu}$ and $1000/Q_S$, blocks near the surface layer show high resolution (resolution matrix diagonals >0.9), as do those in the mantle wedge (40–100 km depth) and the crust directly beneath the array (Figure 11). Lower resolution diagonals are observed for the subducting lithosphere below the earthquakes (<0.7) and in the northernmost part of the mantle wedge (<0.5, all depths). This pattern reflects ray coverage. Rays sample the mantle wedge by short and crossing paths between the intermediate-depth earthquakes and the stations, but sample the downgoing plate only by long along-strike paths and just near its upper surface. $1000/Q_{Pc}$ shows a similar pattern except below 80 km depth, where the positivity constraint dominates and resolution is low. Formal errors show a pattern similar to resolution, modified by variations of a priori constraints, as expected [*Jackson*, 1979].

5.3.3. Numerical Resolution Tests

[39] Numerical tests also demonstrate the recovery of features. In each, we trace the ray paths for all station-event pairs through a simple $1000/Q$ model to generate synthetic data, with structure resembling features of interest, and then invert these predicted t^* values in the same manner as real data, to recover the simple model. We discuss Q_S results; Q_P is similar.

[40] A checkerboard test (Figure 12a) shows that features of 20 km dimension can be resolved through much of the wedge, in the volume between the slab seismicity and the stations. Amplitude recovery in the northern part of the wedge is roughly 80% beneath the stations, falling off rapidly to the north. Structure below the seismic zone shows relatively poorer recovery. The high-attenuation region of the slab <80 km deep appears to be well resolved.

[41] A second test (Figure 12b) simulates the effect of a high-attenuation mantle wedge. Where resolution is high,

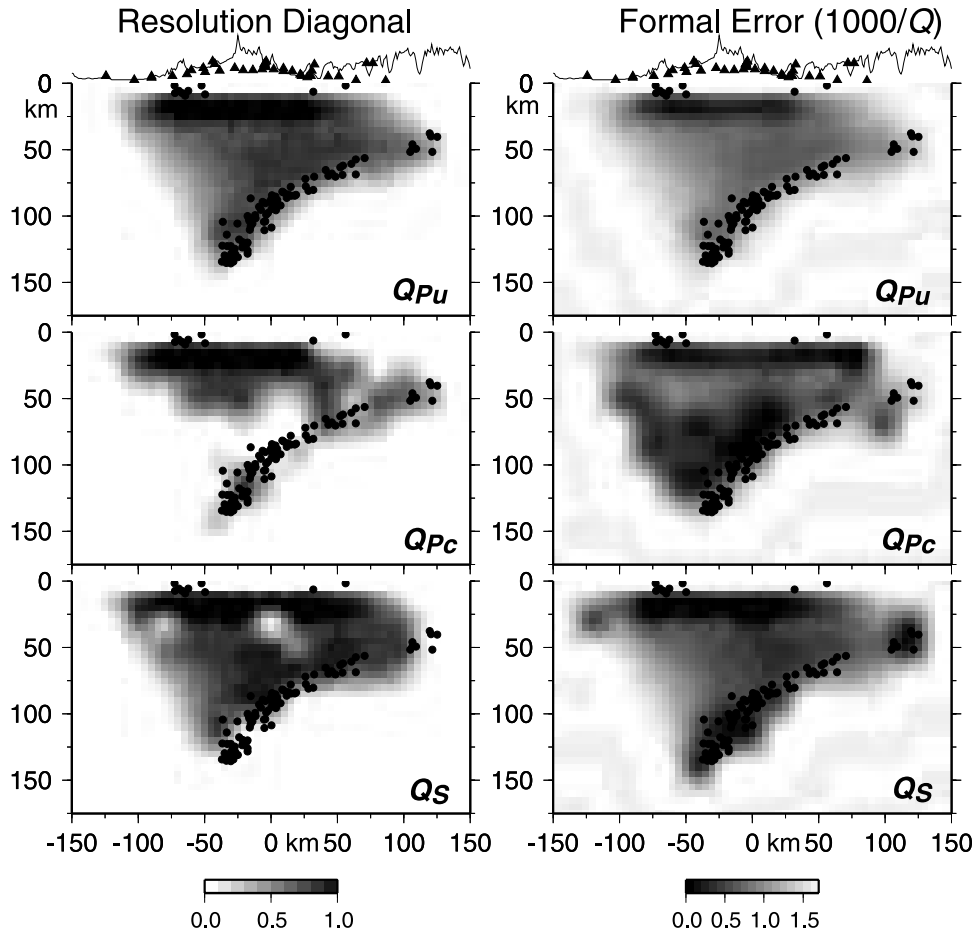

Figure 11. Formal resolution and error estimates from inversions for cross section shown in Figure 10. (left) Diagonals of resolution matrix. (right) Full a posteriori uncertainty in units of $1000/Q$. Q_{Pu} is unconstrained P wave inversion; Q_{Pc} is P wave inversion constrained so Q_κ is nonnegative; Q_S is S wave inversion.

$1000/Q_S$ differs by <30% between initial and recovered models. Recovery rapidly decays away from the region of high-resolution matrix diagonals.

5.4. Minimal Parameterization

[42] We also invert t^* for a minimum parameterization model (Figure 13). Here, we solve for six irregularly shaped blocks in the central part of the array (plus the near-surface layer described above), generated in the manner of *Abers and Roecker* [1991]. These blocks are divided in three along strike, in the manner of Figure 9, although most distal blocks are not sampled. This parameterization has the advantage that all blocks are overdetermined and that $1000/Q$ is resolved nearly perfectly (resolution diagonals >0.98 for all blocks shown). This inversion shows, for the mantle wedge, $1000/Q_S = 9.1 \pm 0.5$ (2σ uncertainty; $Q_S = 110 \pm 5.5\%$). This value is 20% higher than $1000/Q_{\text{av-cor}}$ (Table 1), presumably because ray segments outside the wedge are better accounted for. For the crust this inversion gives $1000/Q_S = 1.63$ ($Q_S = 613 \pm 9.8\%$) and for the deeper slab $1000/Q_S \ll 0.1$. While these results depend somewhat on the exact position of the block boundaries (shifts by 1/2 of the grid spacing result in 10–20% changes in $1000/Q_S$), they generally support the values derived from other means.

6. Discussion

6.1. Subduction Zone Structure

[43] The attenuation structure imaged here (Figures 10 and 14) resembles that of many subduction zones, albeit with high resolution. The mantle wedge shows high attenuation, while the deeper parts of the slab show little. Velocity tomography shows a similar pattern [*Zhao et al.*, 1995]. Unexpectedly, shallower parts of the slab show a region of moderate attenuation. The upper plate crust shows relatively little attenuation in S although more in P, which (as discussed below) indicates a nonthermal dissipative process. The mantle wedge here appears similar in geometry and $1/Q_S$ with other subduction zones which have volcanic arcs (Table 2), from which we conclude that the thermal structure and flow field beneath the Alaska Range are grossly similar to them.

[44] The high-attenuation part of the mantle wedge seems confined to the area where the slab seismicity lies at depths greater than 80 km, below or northwest of the high elevation of the Alaska Range (Figure 10). The part of the wedge to

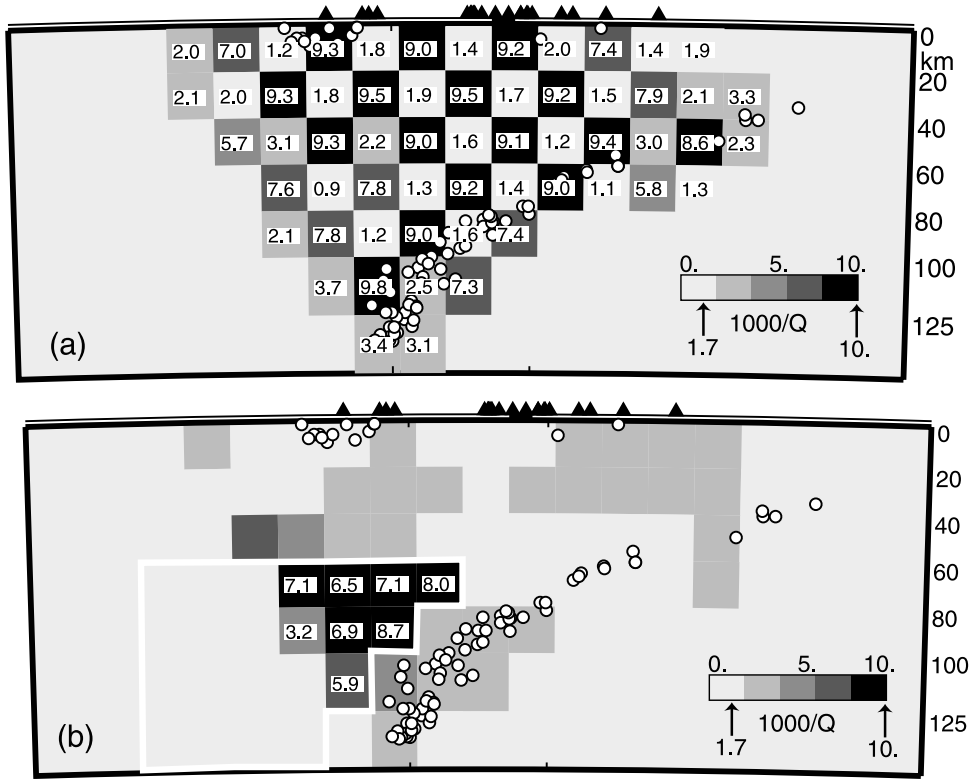

Figure 12. Numerical resolution tests. (a) Checkerboard resolution test. Starting checkerboard has 20 km blocks in two dimensions, with $1000/Q$ alternating between the a priori value, 1.7, and 10. Note good recovery throughout region. (b) High-attenuation mantle wedge test. Attenuation measurements generated $1000/Q = 10$ in wedge, bound by white line, and 1.7 elsewhere. Both tests use same rays and uncertainties as actual Q_S result. Circles show events; triangles show stations. Blocks labeled with $1000/Q$ if resolution diagonals exceed 0.01 (only within wedge for Figure 12b). This is same cross section as Figure 10. For well-resolved blocks, amplitude recovery is 69–87%.

the southeast, where the slab is shallower, shows moderate to high $1/Q$. A similar pattern has been observed in northern Japan [*Takanami et al.*, 2000] and likely typifies many subduction zones. The simplest explanation is that the low-Q zone represents hot flowing mantle, while the high-Q mantle is a cold, viscous nose of the wedge that is isolated from large-scale flow, consistent with numerical experiments [*Kincaid and Sacks*, 1997]. Partial serpentinization of this cold, shallow part of the wedge would increase its buoyancy and further increase its resistance to flow. The boundary between high- and low-Q wedges also corresponds with a 90° rotation in mantle anisotropy inferred from shear wave splitting [*Christensen et al.*, 2003], supporting the inference that marks a boundary between flow regimes. The boundary lies along the southern margin of the Alaska Range, a major mountain belt actively forming well inland of the subduction zone. Perhaps, the contrast in strength between hot and cold mantle, inferred from attenuation, provides a control on localization of strain here.

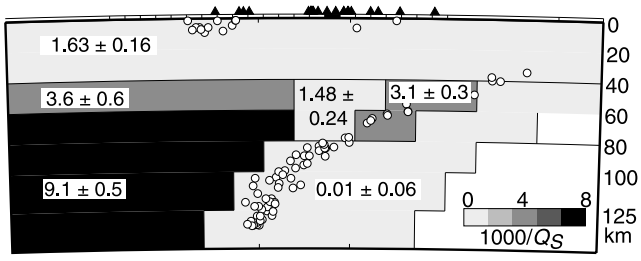

Figure 13. Minimum parameter inversion for $1000/Q_S$. Format is the same as Figure 10. Formal errors are 2σ.

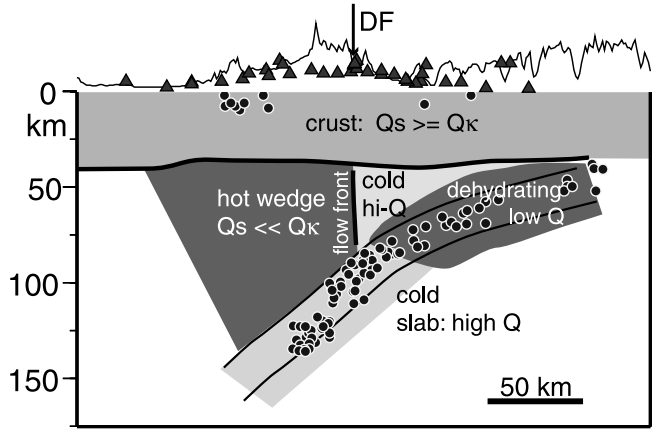

Figure 14. Cartoon illustrating main Q regimes. DF shows Denali Fault trace.

Table 2. Q Measurements in Centers of Mantle Wedges, 50–100 km Depth

Region	Q_P	Q_S	Band,[a] Hz	α	Reference
Central Alaska	537 ± 193	283 ± 57	0.3–9(S), 1–19(P)	0	this study
Central Alaska	266 ± 51	138 ± 11	0.3–9(S), 1–19(P)	0.27	this study
Central Alaska	-	141[b] ± 25	0.3–9(S), 1–19(P)	0	this study, from δt*
Central Alaska	205–345	95–140	0.3–9(S), 1–19(P)	0.27	this study, tomography
Central Alaska	218 ± 10	110 ± 6	0.3–9(S), 1–19(P)	0.27	this study, minimum parameter
NE Japan	150	-	1.0–20?[c]	0	*Tsumura et al.* [2000]
NE Japan	-	70–120[b]	1.0–8.0	0	*Takanami et al.* [2000]
Andes	300	100	0.8–5	0	*Myers et al.* [1998]
Andes	80–150	-	1 to (7–30)	0	*Schurr et al.* [2003]
Tonga (Lau Basin)	240	-	1.0–7.6	0	*Bowman* [1988]
Tonga (Lau Basin)	120–121	45–57	0.05–0.5	0.1–0.3	*Flanagan and Wiens* [1998]
Tonga (Lau Basin)	90[b]	-	0.1–3.5	0	*Roth et al.* [1999]

[a]Characteristic frequency band sampled; numerical experiments indicate that Q is measured at the upper end of this band.
[b]Based on S-to-P spectral ratios.
[c]Estimated from figures of *Tsumura et al.* [2000].

Regardless, a prominent lateral boundary divides the wedge between a shallow, presumably cold region to the south, and the hot region that comprises most of its volume.

[45] All inversions show a well-resolved region of high attenuation within the slab, where slab seismicity lies at shallow depths of 40–80 km. This part of the subducting plate has been shown from receiver functions to consist of a thick low-velocity layer, 14–22 km wide, probably crust of a subducting exotic terrane that has not converted to eclogite [*Ferris et al.*, 2003]. Over the 40–80 km depth range the seismic velocities within the layer increase significantly with increasing depth, perhaps indicating that the oceanic crust is dehydrating. The breakdown of hydrous minerals in subducted crust introduces free H_2O to the region, which could significantly affect shear and perhaps bulk moduli, depending upon crack geometry and density [e.g., *Schmeling*, 1985; *Takei*, 2002]. The imaged high-attenuation region corresponds closely to the subducted crust.

6.2. Q_κ-Q_μ Relationship and Physical Mechanism

[46] Four distinct regimes can be defined on the basis of $1/Q_\kappa$ and $1/Q_S$ ($1/Q_\mu$): (1) a hot mantle wedge, with high $1/Q_\mu$ and near-zero $1/Q_\kappa$; (2) a cold slab >80 km deep with generally low attenuation; (3) an upper crust with low but variable $1/Q_\mu$ and moderate $1/Q_\kappa$; and (4) an unusual portion of the slab <80 km deep with moderate to high $1/Q_\mu$ and $1/Q_\kappa$. The $(1/Q_\kappa)/(1/Q_\mu)$ ratio (Figure 15) shows strong changes across the Moho of the upper plate, and at the top of the downgoing plate as inferred from seismicity. In the intervening mantle wedge, $1/Q_\kappa \ll 1/Q_\mu$, while in both the downgoing and overlying crust, $1/Q_\kappa$ is relatively significant. These variations are unlikely to be due to varying resolution because the P and S inversions use exactly the same ray paths for identical sets of source-receiver pairs.

[47] The mantle wedge exhibits high $1/Q_\mu$, negligible $1/Q_\kappa$, and frequency dependence consistent with $\alpha = 0.27$. These observations validate the application here of thermally activated, high-temperature background attenuation models derived from laboratory data [*Jackson et al.*, 2002; *Karato*, 2003]. While these mechanisms are often assumed to be applicable [*Nakajima and Hasegawa*, 2003], such supporting observations are rarely available. By contrast, no such theory can be applied to the other regions where $1/Q_\kappa$ is significant, and interpretation is necessarily qualitative. For example, the shallow portion of the slab may have elevated $1/Q_\kappa$ and $1/Q_\mu$ because fluids are abundant, as discussed above, but it is difficult to constrain the fluid content or pore geometry needed to produce the observations.

[48] In both the upper plate crust and descending crust $1/Q_\kappa$ is significant, indicating that some other mechanism must be attenuating seismic waves. Possibly scattering may play a role. However, the Q_S for the crust inferred here is similar in both value and α to that inferred from *Lg* and from coda [*McNamara*, 2000], despite the differences in how these wave types sample the scattered wave field. This similarity indicates intrinsic effects dominate Q [*Sarker and Abers*, 1998a]. As discussed above, poorly consolidated basin sediments may affect parts of the crustal signal, as might an abundance of fractures or fluid circulation in tectonically active regions.

[49] In the slab and perhaps crust, it is possible that heterogeneous materials exhibit significant thermoelasticity, a mechanism that should affect $1/Q_\kappa$ strongly [*Budiansky et al.*, 1983; *Heinz et al.*, 1982]. Although this mechanism is not thought to be important most places in the Earth, in cold slabs the normal thermal mechanisms affecting Q_μ should be unimportant, so other processes may dominate. In heterogeneous materials, thermoelastic attenuation derives

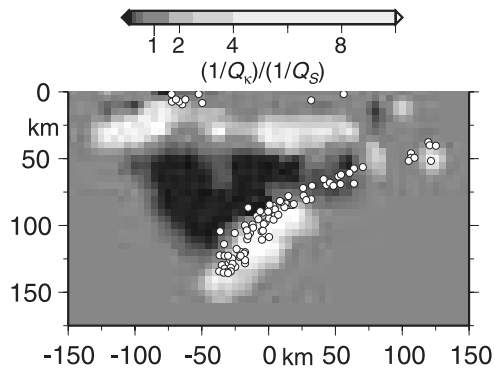

Figure 15. Attenuation ratio for bulk modulus to shear modulus from division of images in Figure 10. In mantle wedge, bulk modulus attenuation is negligible, while it is significant in the crust and descending plate. See color version of this figure at back of this issue.

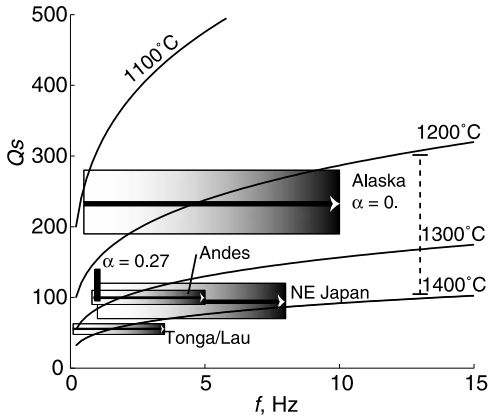

Figure 16. Comparison of observed Q_S in sub-arc mantle (Table 2) with predictions. Observations are from NE Japan [*Takanami et al.*, 2000], Andes [*Myers et al.*, 1998], Tonga/Lau [*Roth et al.*, 1999], or this study (Alaska; $\alpha = 0.27$). Horizontal box width denotes frequencies sampled. All except Alaska assume $\alpha = 0$, so likely reflect Q_S at the high end of the frequency range sampled (darkest shading). Alaska wedge appears ~100°C cooler than Andes or NE Japan. Predictions are from calibration of *Jackson et al.* [2002] for 1 mm grain size, adjusted to 2.5 GPa (80 km depth) as described in text. Increasing grain size to 10 mm increases predictions by 100°C, ignoring activation volume decreases predictions 130°C. Dashed line shows typical error in absolute temperature for 1300°C; relative errors are much smaller. Abundant H_2O would lower actual temperatures [*Karato*, 2003].

from differences in compressibility and thermal conductivity between components in polycrystalline aggregates. Although anhydrous mantle is predicted to have $Q_\kappa \sim 5000$ from this process [*Heinz et al.*, 1982], the process is not well understood. The presence of hydrous phases and isolated free fluid pockets could greatly enhance the grain-scale heterogeneity of subducting slabs, which in turn could increase $1/Q_\kappa$ through this effect. These mechanisms should have frequency dependence of $\alpha = 0.5$ [*Budiansky et al.*, 1983], consistent with slab paths here (Figure 6).

6.3. Inferred Temperature and Comparison With Other Arcs

[50] In the mantle wedge, the BEAAR data indicate $Q_S \sim 100-150$ at 1 Hz for $\alpha = 0.27$ (Table 1 and Figures 10 and 13). To compare these results with those from other studies, which commonly assume $\alpha = 0$, our Q estimates for the wedge should be multiplied by 2.0 ($Q_S = 125$ gives $f_R = 10$ Hz; see section 4.4.3). The conversion depends upon the maximum frequency (f_R) used to measure Q, which likely varies from study to study, so values are not directly comparable unless f_R is similar. Still, compared with other arcs, the wedge beneath Alaska appears to be less attenuating (Table 2 and Figure 16).

[51] To estimate temperature (T), we assume that the high-T background model for Q applies to the wedge, as measured by the laboratory experiments of *Jackson et al.* [2002], and that H_2O content or grain size variations can be ignored. Temperatures are calculated at a depth of 80 km (2.45 GPa), assuming an activation volume of 13.8 cm^3/mol derived from comparing Q to T globally [*Abers et al.*, 2003]. This pressure correction increases T estimates by 130°C from laboratory values (at 0 GPa), and lies within the range of laboratory estimates for activation volume [*Hirth and Kohlstedt*, 2003]. For a nominal grain size of 1 mm, the Alaska results indicate $T \sim 1250$°C with 25–50° uncertainties, both from the $\alpha = 0.27$ results at 1 Hz and from the $\alpha = 0$ results at 10 Hz. Changes in grain size, activation volume, or water content would change these absolute estimates, typically on the order of 100°C, but the relative variations in T do not change much. Results from other wedges, compared at the highest frequency sampled, show T to be 100°C higher for the Andes and NE Japan, still below the dry solidus of 1420°C at 2.45 GPa [*Hirschmann*, 2000] but hot enough to allow some wet melting.

[52] *Nakajima and Hasegawa* [2003] also estimated T from Q_P in the hottest part of the mantle wedge in NE Japan. They assume a similar relationship between Q_S and T as do we, but use T and pressure measured from sub-arc mantle xenoliths to calibrate the absolute scale. They implicitly assume that Q in all parts of their model reflects the same dominant frequency. This approach gives somewhat lower T than Figure 16, by about 140°C for Alaska, although relative variations in T between arcs are similar to ours within 10°C. The cause of the discrepancy is unclear, but may be due to the presence of water in subduction zones as H^+ impurities within olivine grains. If this effect is ignored, as we do, but H+ is present, the T inferred by our method should be overestimated by on the order of 100°C at normal mantle-wedge water contents [*Karato*, 2003]. It is also possible that the xenoliths underestimate T, if for example the pressures are overestimated.

[53] We have no reason to think that water contents vary significantly between arcs, so the Alaska wedge appears to be colder than others beneath active arcs, by 100 ± 30°C. A cold wedge in Alaska could explain the lack of arc volcanism above the slab here. One small young volcanic feature has been found, the Buzzard Creek Maar on the north slope of the Alaska range just east of the BEAAR transect [*Nye*, 1999], but elsewhere Quaternary volcanism is absent on Figure 1. Perhaps low temperatures in some way result from the flow geometry set up by the unusually flat slab and long distance to the trench. Alternatively, thickening of the upper plate lithosphere, associated with building the Alaska Ranges, may depress the hot part of the mantle wedge to depths below those where dehydration occurs. In any case, the low temperatures inferred from Q_S, compared with other subduction zones, could explain the absence of volcanism beneath central Alaska.

7. Conclusions

[54] The BEAAR data set provides some of the highest-resolution information on attenuation at mantle depths found in any subduction zone, comparable to the resolution of images obtained for seismic velocities. The data can independently constrain attenuation of S and P waves, making it possible to separately evaluate the importance of attenuation in shear modulus ($1/Q_\mu$) and bulk modulus ($1/Q_\kappa$). Tests show that direct, parametric fits to spectra (with equation (2)) give estimates of t^* that are as accurate as any

other method, making the separate determination of S and P attenuation possible. The spectra also show significant sensitivity to the frequency dependence of attenuation and show that frequency dependence is required to explain observations. These two characteristics of this data set allow the mechanism of intrinsic attenuation to be assessed rather than assumed, and show that thermally activated high-temperature processes can explain attenuation in the mantle wedge part of the subduction zone, where $\alpha \sim 0.27$ and $1/Q_\kappa \sim 0$. Elsewhere, we find higher frequency dependence and significant $1/Q_\kappa$, requiring other attenuative processes.

[55] The results show a high-attenuation mantle wedge overlying the subducting slab, at least where seismicity is >80 km deep, consistent with subduction zones elsewhere. The wedge over the shallower part of the slab shows low attenuation, consistent with the notion of a stagnant viscous nose developing there. The deeper part of the slab shows very little attenuation, as expected. These characteristics show that to first order the thermal structure of the Alaska subduction zone resembles that of subduction zones elsewhere, despite the absence of arc volcanism. An unusual region of moderate to high attenuation in both $1/Q_\mu$ and $1/Q_\kappa$ exists within the subducting slab, probably within the subducting crust, where it is less than 80 km depth. In this region, an unusually thick crustal section is subducting and likely dehydrating, providing conditions for high attenuation despite presumably low temperatures.

[56] Although the overall pattern of attenuation appears similar to that seen in other arcs, the highest values of $1/Q_S$ are roughly half those observed beneath other arcs, once effects of frequency dependence are taken into account. This difference is probably best explained by a colder mantle wedge above the Alaska slab, by roughly 100–150° compared with the central Andes or northern Japan. These unusually low temperatures may explain the absence of arc volcanism over this otherwise normal subducting plate.

[57] **Acknowledgments.** The BEAAR project would not have been successful without the help of many people, in particular, L. Meyers, who kept instruments operating year-round; the staff of the PASSCAL Instrument Center (PIC); and A. Ferris, who assisted in data processing. Instruments were made available through the PIC operated by IRIS. IRIS also supported a summer intern. R. Hansen and Alaska Earthquake Information Center made network arrival time data available throughout the experiment. This paper benefited from discussions with R. Abercrombie and G. Hirth and thoughtful reviews by A. Shito and M. Flanagan and Associate Editor S. Karato. This work was funded by NSF grant EAR9996461 to Boston University.

References

Abercrombie, R. E. (1995), Earthquake source scaling relationships from −1 to 5 M_L using seismograms recorded at 2.5-km depth, *J. Geophys. Res.*, *100*, 24,015–24,036.

Abercrombie, R. E. (1997), Near-surface attenuation and site effects from comparison of surface and deep borehole recordings, *Bull. Seismol. Soc. Am.*, *87*, 731–744.

Abers, G. A., and S. Roecker (1991), Deep structure of an arc-continent collision: Earthquake relocation and inversion for upper mantle *P* and *S* wave velocities beneath Papua New Guinea, *J. Geophys. Res.*, *96*, 6379–6401.

Abers, G. A., and G. Sarker (1996), Dispersion of regional body waves at 100–150 km depth beneath Alaska: In situ constraints on metamorphism of subducted crust, *Geophys. Res. Lett.*, *23*, 1171–1174.

Abers, G. A., J. C. Stachnik, and D. H. Christensen (2003), Constraints on the mechanism of attenuation and thermal structure in subduction zones: Results from BEAAR, *Eos Trans. AGU*, *84*(46), Fall Meet. Suppl., Abstract S22B-0452.

Aki, K., and P. G. Richards (1980), *Quantitative Seismology: Theory and Methods*, 557 pp., W. H. Freeman, New York.

Anderson, J. G. (1986), Implication of attenuation for studies of earthquake sources, in *Earthquake Source Mechanics*, *Geophys. Monogr. Ser.*, vol. 37, edited by S. Das, J. Boatwright, and C. H. Scholz, pp. 311–318, AGU, Washington, D. C.

Anderson, J. G., and S. E. Hough (1984), A model for the shape of the Fourier amplitude spectrum of acceleration at high frequencies, *Bull. Seismol. Soc. Am.*, *74*, 1969–1993.

Aster, R. C., and P. M. Shearer (1991), High-frequency borehole seismograms recorded in the San Jacinto Fault Zone, southern California, part 2. Attenuation and site effects, *Bull. Seismol. Soc. Am.*, *81*, 1081–1100.

Benz, H. M., A. Frankel, and D. M. Boore (1997), Regional *Lg* attenuation for the continental United States, *Bull. Seismol. Soc. Am.*, *87*, 606–619.

Bowman, J. R. (1988), Body wave attenuation in the Tonga subduction zone, *J. Geophys. Res.*, *93*, 2125–2139.

Budiansky, B., E. E. Sumner, and R. J. O'Connell (1983), Bulk thermoelastic attenuation of composite materials, *J. Geophys. Res.*, *88*, 10,343–10,348.

Christensen, D. H., G. A. Abers, and T. McNight (2003), Mantle anisotropy beneath the Alaska Range inferred from *S*-wave splitting observations: Results from BEAAR, *Eos Trans. AGU*, *84*(46), Fall Meet. Suppl., Abstract S31C-0782.

Dziewonski, A. M., and D. L. Anderson (1981), Preliminary reference Earth model, *Phys. Earth Planet. Inter.*, *25*, 297–356.

Eberhart-Phillips, D., and M. Chadwick (2002), Three-dimensional attenuation model of the shallow Hikurangi subduction zone in the Raukumara Peninsula, New Zealand, *J. Geophys. Res.*, *107*(B2), 2033, doi:10.1029/2000JB000046.

Elkins-Tanton, L. G., T. L. Grove, and J. Donnelly-Nolan (2001), Hot shallow mantle melting under the Cascades volcanic arc, *Geology*, *29*, 631–634.

Ferris, A., G. A. Abers, D. H. Christensen, and E. Veenstra (2003), High resolution image of the subducted Pacific (?) plate beneath central Alaska, 50–150 km depth, *Earth Planet. Sci. Lett.*, *214*, 575–588.

Flanagan, M. P., and D. A. Wiens (1994), Radial upper mantle attenuation structure of inactive back arc basins from differential shear wave measurements, *J. Geophys. Res.*, *99*, 15,469–15,486.

Flanagan, M. P., and D. A. Wiens (1998), Attenuation of broadband *P* and *S* waves in Tonga: Observations of frequency dependent *Q*, *Pure Appl. Geophys.*, *153*, 345–375.

Haberland, C., and A. Rietbrock (2001), Attenuation tomography in the western central Andes: A detailed insight into the structure of a magmatic arc, *J. Geophys. Res.*, *106*, 11,151–11,167.

Heinz, D., R. Jeanloz, and R. J. O'Connell (1982), Bulk attenuation in a polycrystalline Earth, *J. Geophys. Res.*, *87*, 7772–7778.

Hirschmann, M. (2000), Mantle solidus: Experimental constraints and the effects of peridotite composition, *Geochem. Geophys. Geosyst.*, *1*, paper 2000GC000070.

Hirth, G., and D. Kohlstedt (2003), Rheology of the upper mantle and mantle wedge: A view from the experimentalists, in *Inside the Subduction Factory*, *Geophys. Monogr. Ser.*, vol. 138, edited by J. M. Eiler, pp. 83–106, AGU, Washington, D. C.

Hough, S. E., J. G. Anderson, J. Brune, I. F. Vernon, J. Berger, J. Fletcher, L. Haar, T. Hanks, and L. Baker (1988), Attenuation near Anza, California, *Bull. Seismolon. Soc. Am.*, *78*, 672–691.

Jackson, D. D. (1979), The use of a priori data to resolve non-uniqueness in linear inversion, *Geophys. J. R. Astron. Soc.*, *57*, 137–157.

Jackson, I., M. S. Paterson, and J. D. F. Gerald (1992), Seismic wave dispersion and attenuation in Aheim dunite: An experimental study, *Geophys. J. Int.*, *108*, 517–534.

Jackson, I., J. D. FitzGerald, U. H. Faul, and B. H. Tan (2002), Grain-size-sensitive seismic wave attenuation in polycrystalline olivine, *J. Geophys. Res.*, *107*(B12), 2360, doi:10.1029/2001JB001225.

Karato, S. (1993), Importance of anelasticity in the interpretation of seismic tomography, *Geophys. Res. Lett.*, *20*, 1623–1626.

Karato, S. (2003), Mapping water content in the upper mantle, in *Inside the Subduction Factory*, *Geophys. Monogr. Ser.*, vol. 138, edited by J. M. Eiler, pp. 135–152, AGU, Washington, D. C.

Karato, S., and H. A. Spetzler (1990), Defect microdynamics in minerals and solid-state mechanisms of seismic wave attenuation and velocity dispersion in the mantle, *Rev. Geophys.*, *28*, 399–421.

Kelemen, P. B., J. L. Rilling, E. M. Parmentier, L. Mehl, and B. R. Hacker (2003), Thermal structure due to solid-state flow in the mantle wedge beneath arcs, in *Inside the Subduction Factory*, *Geophys. Monogr. Ser.*, vol. 138, edited by J. M. Eiler, pp. 293–311, AGU, Washington, D. C.

Kincaid, C., and I. S. Sacks (1997), Thermal and dynamical evolution of the upper mantle in subduction zones, *J. Geophys. Res.*, *102*, 12,295–12,315.

Kirschner, C. E. (1994), Interior basins of Alaska, in *The Geology of North America*, vol. G-1, *The Geology of Alaska*, edited by G. Plafker and H. C. Berg, pp. 469–493, Geol. Soc. of Am., Boulder, Colo.

Lindquist, K. G. (1998), Seismic array processing and computational infrastructure for improved monitoring of Alaskan and Aleutian seismicity and volcanoes, Ph.D. thesis, Univ. of Alaska, Fairbanks.

Madariaga, R. (1976), Dynamics of an expanding circular fault, *Bull. Seismol. Soc. Am.*, *66*, 639–666.

McNamara, D. E. (2000), Frequency dependent Lg attenuation in south-central Alaska, *Geophys. Res. Lett.*, *27*(23), 3949–3952.

Meyers-Smith, E. V., D. H. Christensen, and G. Abers (2002), Moho topography beneath the Alaska Range: Results from BEAAR, *Eos Trans. AGU*, *83*(47), Fall Meet. Suppl., Abstract S52A-1073.

Mitchell, B. J. (1995), Anelastic structure and evolution of the continental crust and upper mantle from seismic surface wave attenuation, *Rev. Geophys.*, *33*, 441–462.

Myers, S. C., S. Beck, G. Zandt, and T. Wallace (1998), Lithospheric-scale structure across the Bolivian Andes from tomographic images of velocity and attenuation for *P* and *S* waves, *J. Geophys. Res.*, *103*, 21,233–21,252.

Nakajima, J., and A. Hasegawa (2003), Estimation of thermal structure in the mantle wedge of northeastern Japan from seismic attenuation data, *Geophys. Res. Lett.*, *30*(14), 1760, doi:10.1029/2003GL017185.

Nye, C. J. (1999), The Denali volcanic gap—Magmatism at the eastern end of the Aleutian Arc, *Eos Trans. AGU*, *80*(46), Fall Meet. Suppl., F1202.

O'Connell, R. J., and B. Budiansky (1977), Viscoelastic properties of fluid-saturated cracked solids, *J. Geophys. Res.*, *82*, 5719–5735.

Park, J., C. R. Lindberg, and I. F. Vernon (1987), Multitaper spectral analysis of high-frequency seismograms, *J. Geophys. Res.*, *92*, 12,675–12,684.

Plafker, G., and H. C. Berg (1994), Overview of the geology and tectonic evolution of Alaska, in *The Geology of North America*, vol. G-1, *The Geology of Alaska*, edited by G. Plafker and H. C. Berg, pp. 989–1021, Geol. Soc. of Am., Boulder, Colo.

Plafker, G., L. M. Gilpin, and J. Lahr (1994), Neotectonic map of Alaska, in *The Geology of North America*, vol. G-1, *The Geology of Alaska*, edited by G. Plafker and H. C. Berg, Plate 12, Geol. Soc. of Am., Boulder, Colo.

Rautian, T. G., V. I. Khalturin, V. G. Martynov, and P. Molnar (1978), Preliminary analysis of the spectral content of *P* and *S* waves from local earthquakes in the Garm, Tadjikistan region, *Bull. Seismol. Soc. Am.*, *68*(4), 949–971.

Roecker, S. W. (1993), Tomography in zones of collision: Practical considerations and examples, in *Seismic Tomography Theory and Practice*, edited by H. M. Iyer and K. Hirahara, pp. 534–611, Chapman and Hall, New York.

Roth, E. G., D. A. Wiens, L. M. Dorman, J. Hildebrand, and S. C. Webb (1999), Seismic attenuation tomography of the Tonga back-arc region using phase pair methods, *J. Geophys. Res.*, *104*, 4795–4809.

Sarker, G., and G. A. Abers (1998a), Comparison of seismic body wave and coda wave measures of *Q*, *Pure Appl. Geophys.*, *153*, 665–683.

Sarker, G., and G. A. Abers (1998b), Deep structures along the boundary of a collisional belt: Attenuation tomography of *P* and *S* waves in the Greater Caucasus, *Geophys. J. Int.*, *133*, 326–340.

Sato, H., I. Sacks, T. Murase, G. Muncill, and H. Fukuyama (1989), Qp-melting temperature relation in peridoite at high pressure and temperature: Attenuation mechanism and implications for the mechanical properties of the upper mantle, *J. Geophys. Res.*, *94*, 10,647–10,661.

Schlotterbeck, B. A., and G. A. Abers (2001), Three-dimensional attenuation variations in southern California, *J. Geophys. Res.*, *106*, 30,719–30,735.

Schmeling, H. (1985), Numerical models on the influence of partial melt on elastic, anelastic and electric properties of rocks, part I: Elasticity and anelasticity, *Phys. Earth Planet. Inter.*, *41*, 34–57.

Schurr, B., G. Asch, A. Rietbrock, R. Trumbull, and C. Haberland (2003), Complex patterns of fluid and melt transport in the central Andean subduction zone revealed by attenuation tomography, *Earth Planet. Sci. Lett.*, *215*, 105–119.

Shito, A., S. Karato, and J. Park (2004), Frequency dependence of *Q* in Earth's upper mantle inferred from continuous spectra of body waves, *Geophys. Res. Lett.*, *31*, L12603, doi:10.1029/2004GL019582.

Stachnik, J. C. (2002), Seismic attenuation in central Alaska, M.A. thesis, Boston Univ., Boston, Mass.

Takanami, T., S. Sacks, and A. Hasegawa (2000), Attenuation structure beneath the volcanic front in northeastern Japan from broad-band seismograms, *Phys. Earth Planet. Inter.*, *121*, 339–357.

Takei, Y. (2002), Effect of pore geometry on V_P/V_S: From equilibrium geometry to crack, *J. Geophys. Res.*, *107*(B2), 2043, doi:10.1029/2001JB000522.

Tarantola, A. (1987), *Inverse Problem Theory: Methods for Data Fitting and Model Parameter Estimations*, 613 pp., Elsevier Sci., New York.

Tarantola, A., and B. Valette (1982), Generalized non-linear inverse problems solved using least squares criterion, *Rev. Geophys.*, *20*, 219–232.

Tsumura, N., S. Matsumoto, S. Horiuchi, and A. Hasegawa (2000), Three-dimensional attenuation structure beneath the northeastern Japanese arc estimated from spectra of small earthquakes, *Tectonophysics*, *319*, 241–260.

Warren, L., and P. Shearer (2000), Investigating the frequency dependence of mantle *Q* by stacking *P* and *PP* spectra, *J. Geophys. Res.*, *105*, 25,391–25,402.

Winkler, K., and A. Nur (1979), Pore fluids and seismic attenuation in rocks, *Geophys. Res. Lett.*, *6*, 1–4.

Zhao, D., D. H. Christensen, and H. Pulpan (1995), Tomographic imaging of the Alaska subduction zone, *J. Geophys. Res.*, *100*, 6487–6504.

G. A. Abers, Department of Earth Sciences, Boston University, 685 Commonwealth Ave., Boston, MA 02215, USA. (abers@bu.edu)

D. H. Christensen, Geophysical Institute, University of Alaska Fairbanks, Fairbanks, AK 99775, USA. (doug@giseis.alaska.edu)

J. C. Stachnik, Alaska Earthquake Information Center, Geophysical Institute, University of Alaska Fairbanks, Fairbanks, AK, USA. (josh@giseis.alaska.edu)

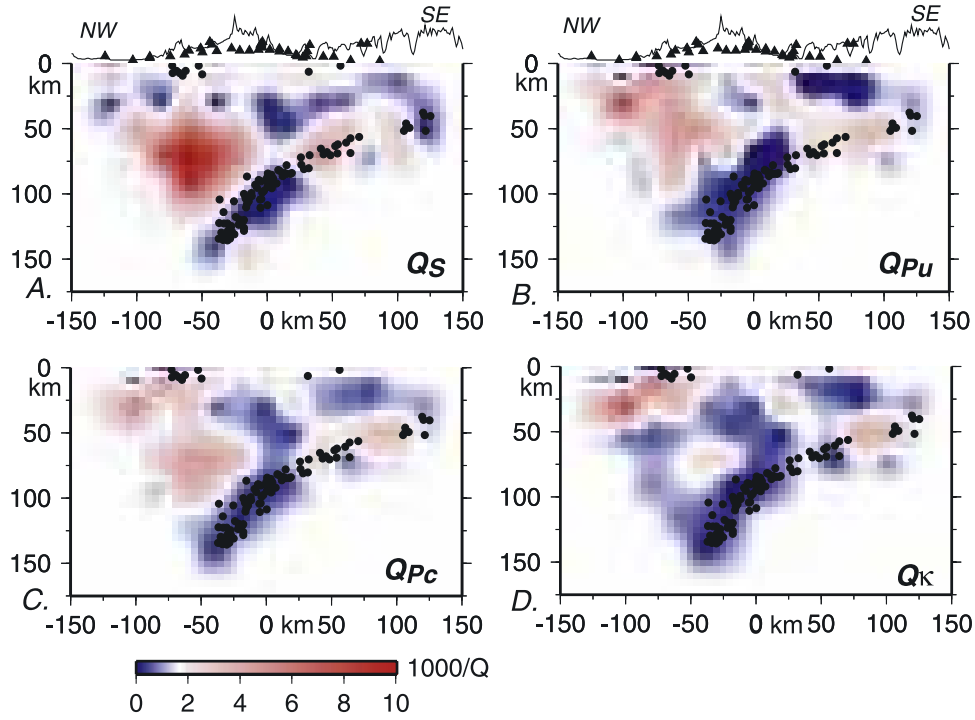

Figure 10. Results of tomographic inversion in cross section (Figure 1): (a) $1000/Q_S$, (b) $1000/Q_P$ with no constraints, (c) $1000/Q_P$ constrained so that $1000/Q_\kappa$ is nonnegative, and (d) resulting bulk modulus attenuation $1000/Q_\kappa$, from equation (1). Circles show events; triangles show stations projected onto cross section. Elevations and topography are exaggerated 10 times. White corresponds to a priori model, $1000/Q = 1.67$ ($Q = 600$).

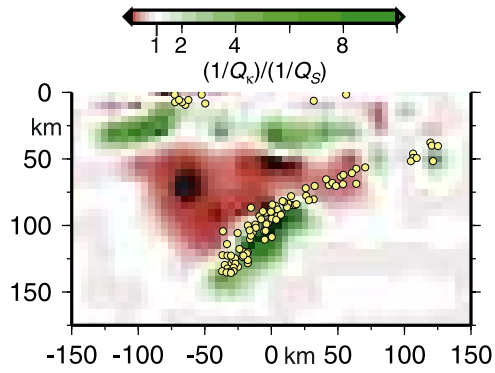

Figure 15. Attenuation ratio for bulk modulus to shear modulus from division of images in Figure 10. In mantle wedge, bulk modulus attenuation is negligible, while it is significant in the crust and descending plate.